Physics of Plasmas

RESEARCH ARTICLE | MARCH 25 2026

Optimizing antihydrogen production via slow plasma merging

E. D. Hunter ; M. Bumbar ; C. Amsler ; M. Bayo ; H. Breuker; M. Cerwenka ; G. Costantini ; R. Ferragut ; M. Giammarchi ; A. Gligorova ; G. Gosta ; M. Hori ; C. Killian ; V. Kraxberger ; N. Kuroda ; A. Lanz ; M. Leali ; G. Maero ; C. Malbrunot ; V. Mascagna ; Y. Matsuda ; S. Migliorati ; D. J. Murtagh ; M. Romé ; R. E. Sheldon ; M. C. Simon ; M. Tajima ; V. Toso ; S. Ulmer ; L. Venturelli ; A. Weiser ; E. Widmann

Check for updates

Phys. Plasmas 33, 032119 (2026)
https://doi.org/10.1063/5.0311707

View Online
Export Citation

Connected Content

A companion article has been published: CERN's faster antihydrogen production enables particle physics insights

Articles You May Be Interested In

Antihydrogen from merged plasmas — cold enough to trap?

AIP Conf. Proc. (October 2006)

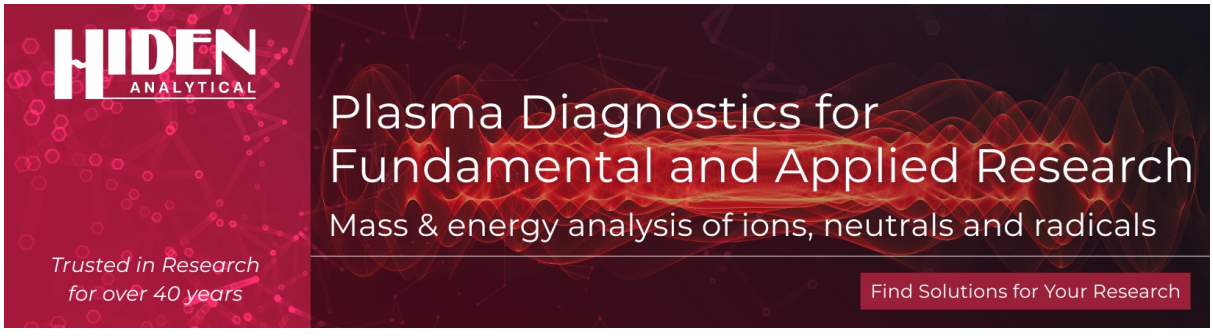
Simulations of plasma confinement in an antihydrogen trap

Phys. Plasmas (October 2007)

Possibilities for achieving antihydrogen recombination and trapping using a nested Penning trap and a magnetic well

Phys. Plasmas (August 2002)

26 October 2026 11:25:02



AIP Publishing

Physics of Plasmas ARTICLE pubs.aip.org/aip/pop

Optimizing antihydrogen production via slow plasma merging

Cite as: Phys. Plasmas **33**, 032119 (2026); doi: 10.1063/5.0311707
Submitted: 11 November 2025 · Accepted: 15 February 2026 ·
Published Online: 25 March 2026

View Online Export Citation CrossMark

E. D. Hunter,[1,2,a] M. Bumbar,[1,2,3] C. Amsler,[4,b] M. Bayo,[5,6] H. Breuker,[7] M. Cerwenka,[3,4,b] G. Costantini,[8,9] R. Ferragut,[5,6] M. Giammarchi,[6] A. Gligorova,[4,c] G. Gosta,[8,9] M. Hori,[2,10] C. Killian,[4,b] V. Kraxberger,[3,4,b] N. Kuroda,[11] A. Lanz,[4,d] M. Leali,[8,9] G. Maero,[6,12] C. Malbrunot,[13] V. Mascagna,[8,9] Y. Matsuda,[11] S. Migliorati,[8,9] D. J. Murtagh,[4] M. Romé,[6,12] R. E. Sheldon,[4,b] M. C. Simon,[4,b] M. Tajima,[2,14] V. Toso,[6,12] S. Ulmer,[7,15] L. Venturelli,[8,9] A. Weiser,[3,b] and E. Widmann[4,b]

AFFILIATIONS

[1]CERN, 1211 Geneva 23, Switzerland
[2]Imperial College, London SW7 2BW, United Kingdom
[3]Vienna Doctoral School in Physics, University of Vienna, 1090 Vienna, Austria
[4]Stefan Meyer Institute for Subatomic Physics, Austrian Academy of Sciences, 1010 Vienna, Austria
[5]L-NESS and Department of Physics, Politecnico di Milano, 22100 Como, Italy
[6]INFN sez. Milano, 20133 Milan, Italy
[7]Ulmer Fundamental Symmetries Laboratory, RIKEN, 351-0198 Saitama, Japan
[8]Dipartimento di Ingegneria dell'Informazione, Università degli Studi di Brescia, 25123 Brescia, Italy
[9]INFN sez. Pavia, 27100 Pavia, Italy
[10]Max-Planck-Institut für Quantenoptik, Hans-Kopfermann-Strasse 1, D85748 Garching, Germany
[11]Institute of Physics, Graduate School of Arts and Sciences, University of Tokyo, 153-8902 Tokyo, Japan
[12]Dipartimento di Fisica, Università degli Studi di Milano, 20133 Milan, Italy
[13]TRIUMF, Vancouver, British Columbia V6T 2A3, Canada
[14]Japan Synchrotron Radiation Research Institute, 1-1-1 Kouto, Sayo-cho, Sayo-gun, 679-5198 Hyogo, Japan
[15]Institut für Experimentalphysik, Heinrich Heine Universität, Düsseldorf, Germany

[a]**Author to whom correspondence should be addressed:** eric.david.hunter@cern.ch
[b]**Current address:** Marietta Blau Institute for Particle Physics, Austrian Academy of Sciences, 1010 Vienna, Austria.
[c]**Current address:** Faculty of Physics, University of Vienna, Boltzmanngasse 5, 1090 Vienna, Austria.
[d]**Current address:** Department of Physics and Astronomy, University College London, Gower Street, London WC1E 6BT, United Kingdom.

ABSTRACT

We present advances in plasma control and diagnosis, leading to the production of exceptionally large quantities of neutral antimatter. We measure the time-dependent temperature and density distribution of antiprotons and positrons while slowly combining them to make antihydrogen atoms in a nested Penning–Malmberg trap. The total antihydrogen yield and the number of atoms escaping the trap as a beam are greatest when the positron temperature is lowest and when antiprotons enter the positron plasma at the smallest radius. We control these parameters by changing the rate at which we lower the electrostatic barrier between the antiproton and positron plasmas and by heating the positrons. With the optimal settings, we produce 2.3×10^6 antihydrogen atoms per 15-min run, surpassing the previous state of the art (3.1×10^4 atoms in 4 min) and the most recent advances in other experiments by factors of 20 and 5, respectively.

© 2026 Author(s). All article content, except where otherwise noted, is licensed under a Creative Commons Attribution (CC BY) license (https://creativecommons.org/licenses/by/4.0/). https://doi.org/10.1063/5.0311707

26 October 2026 11:25:02

© Author(s) 2026

I. INTRODUCTION

The observable universe seems to contain very little antimatter: mostly short-lived decay products in cosmic ray showers, beta-decay positrons, and high energy cosmic rays.[1] In the lab, we can trap a small amount—10^7 antiprotons ($\bar{p}$) or 10^9 positrons (e^+)—as a nonneutral plasma.[2,3] The plasma is confined by electric and magnetic fields in a Penning–Malmberg trap.[4] Four experiments at the CERN antiproton decelerator (AD) presently use such plasmas to produce antihydrogen ($\overline{H}$).[5,6] $\overline{H}$ is neutral,[7] stable,[8] and can be compared with hydrogen spectroscopically[9] and gravitationally.[10] Such comparisons may help to explain the observed excess of matter over antimatter.[11]

Experiments so far use a small fraction ($<10^{-3}$) of the $\overline{H}$ that they produce. Only the coldest atoms, with kinetic energy equivalent to a temperature $T < 0.5$ K, can be trapped by the tesla-scale magnetic bottles used by the ALPHA and ATRAP collaborations.[12,13] T can be higher in beam experiments. The GBAR collaboration plans to create $\overline{H}^+$ ions at a mean kinetic energy of 6 keV ($T \approx 7 \times 10^7$ K). Our collaboration (ASACUSA) plans to measure the ground-state hyperfine structure in a beam of $\overline{H}$.[14] Our spectroscopy apparatus can analyze beams of velocity $v \lesssim 1500$ m/s, corresponding to $T \approx 50$ K.[15] However, the short time (about 1 ms) between $\overline{H}$ formation and analysis means that most atoms in the beam are not in the ground state.[16–18] Moreover, most atoms are not "beam-like" (velocity vector within a few degrees of the trap axis). This motivates our work to increase the number of $\overline{H}$ atoms, to measure their properties shortly after creation, and to control those properties.

In this Paper, we study $\overline{H}$ production and beam formation using the method known as "slow-merge mixing," whereby $\bar{p}$ and e^+ plasmas are combined by adjusting the electrostatic potentials that confine them.[19] We use an order of magnitude more particles of each species to produce 70 times more $\overline{H}$ per run than the previous state of the art,[20] with 70% to 80% of the input $\bar{p}$ forming stable $\overline{H}$. (A "run" is a 15-min sequence of operations to prepare the plasmas, make $\overline{H}$, and diagnose the remaining particles.) We also observe a beam of $\overline{H}$ atoms leaving the trap, which we characterize in another article.[21] Here, we focus on the plasma properties, describing the plasma preparation (and detectors) (Sec. II); time-dependent changes in the plasma density profile, T, and $\overline{H}$ production (Sec. III); the slow extraction of $\bar{p}$ from the plasma (Sec. IV); and the effect of the mixing duration and T of the e^+ (Sec. V). We summarize our findings (Sec. VI) and discuss the analysis of plasma properties (the Appendix).

II. EXPERIMENT

The Cusp trap,[22] shown in Fig. 1(a), is where we combine $\bar{p}$ and e^+ plasmas to make $\overline{H}$. The trap magnetic field B, shown in panel (b), confines the e^+ and $\bar{p}$ radially. The strong gradients in B can focus low-field-seeking atoms[23,24] and do not degrade standard plasma manipulations.[25] We apply time-dependent voltages on hollow cylindrical electrodes to confine and manipulate particles axially. Figure 2(a) shows the trapping fields at the start and end of $\overline{H}$ production. Trap electrodes have inner diameter 34 mm (50 mm for electrodes outside the trapping region). Most trap electrodes have in-trap low-pass filters with time constant $RC \approx 0.01$ ms. Three of the electrodes, 0.05 to 0.25 m away from the middle of the mixing region, do not have filters and are used for plasma compression, heating, pulsed extraction, and transfer. The entrance and exit to the trap are screened by 79% transparent copper meshes to reflect microwave radiation

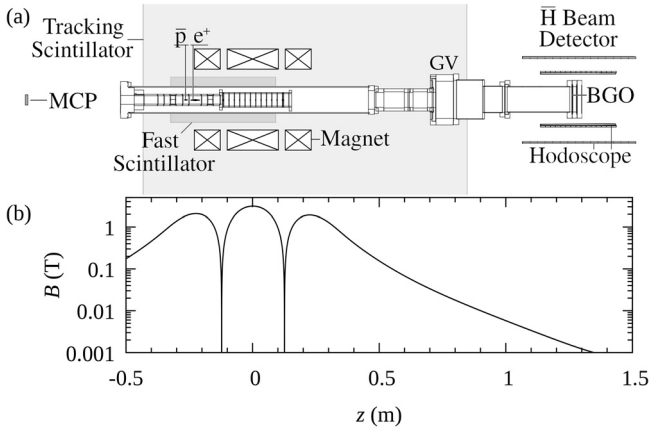


FIG. 1. Simplified cross section of the experiment and calculated magnetic field B along the axis of symmetry. Drawing in (a) is scaled to match the axial position z in (b). The downstream direction corresponds to increasing z. Abbreviations: Scintillating bar arrays (Tracking Scintillator), microchannel-plate phosphor screen (MCP), inner bore scintillator plates (Fast Scintillator), Cusp magnet coils (Magnet), gate valve (GV), and $\overline{H}$ Beam Detector consisting of bismuth germanium oxide crystal (BGO) and scintillating bar layers (Hodoscope). We use the symbols $\bar{p}$ and e^+ for the antiproton and positron plasmas. Microwave meshes at $z = -0.52$ and $+0.48$ m and field ionizers at $z = -0.12$ and $+0.12$ m are not shown.

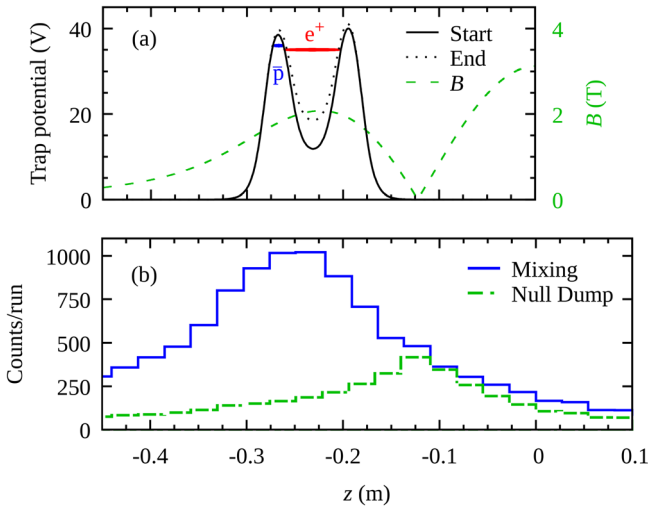


FIG. 2. Trapping potentials and annihilation vertex positions. (a) The electric potential at $r = 0$ generated by the biased electrodes at the start and end of mixing, for the protocol used in Sec. III. B is given again for reference. Length and space charge ϕ of the $\bar{p}$ and e^+ plasmas are suggested by the blue and red ellipses. (b) Vertices found using the Tracking Scintillator during $\overline{H}$ production (Mixing) and slow release downstream (Null dump).

from warm objects outside the 6 K region ($z = -0.5$ to 0.5 m in Fig. 1), which would heat the e^+.[26] The $\bar{p}$ lifetime exceeds 6000 s, implying that the pressure is lower than 10^{-13} mbar.[27]

Figure 1(a) shows the locations of our detectors. We use a single-stage microchannel plate-phosphor screen detector (MCP), with a silicon photomultiplier (SiPM) for diagnosing the plasma temperature T

26 October 2026 11:25:02

© Author(s) 2026

and for counting $\bar{p}$ as in Refs. 28–30. When counting $\bar{p}$, we release particles upstream toward the MCP at $z = -0.9$ m, reducing the confining potential slowly enough to resolve each hit.[31] The detection efficiency is close to 100% (see the Appendix). A CMOS camera records the phosphor screen images, which contain information on the radial distribution of plasma particles.[32] Inside the magnet bore, eight long scintillator plates (Fast Scintillator) record the rate of $\bar{p}$ annihilation in the trap.[31] The Appendix describes our method of calibrating the Fast Scintillator. Outside the magnet, eight arrays of scintillating bars (Tracking Scintillator) track pions generated when $\bar{p}$ annihilate. The distribution of reconstructed annihilations is smeared out by scattering of the pions in the Cusp magnet, yielding a peak position accuracy of about 0.03 m in the axial coordinate z.[33] Figure 2(b) shows the output from the Tracking Scintillator, averaged over 81 runs. Most events are close to the e^+ plasma during mixing and close to the minimum of B when $\bar{p}$ are dumped downstream. The rate limit of the Tracking Scintillator is about 1 kHz, which is too slow for the event rate to be proportional to the true annihilation rate (for which we use the Fast Scintillator). To detect $\bar{H}$ that leave the trap downstream, we use a bismuth germanium oxide crystal (BGO) and two hodoscope layers in 3-coincidence counting mode, as described in Refs. 34 and 21. The BGO-hodoscope combination is called "$\bar{H}$ beam detector" and provides the signal for ASACUSA's spectroscopy program. An average rate of background events—mostly from pions created when $\bar{H}$ annihilates on the trap electrodes—is subtracted using data from runs with the gate valve (GV) closed.

One bunch of 100 keV $\bar{p}$ from the AD's ELENA machine[35] accelerates to 120 keV in ASACUSA's 20 kV pulsed drift tube before hitting a pair of roughly 700-nm-thick degrader foils.[36] We capture 25% of the bunch, or about 3×10^6 $\bar{p}$ per AD cycle. The $\bar{p}$ from multiple AD cycles can be collected in our catching trap.[2] We take either three bunches (Secs. III and IV) or 1 bunch (Sec. V) before compressing the $\bar{p}$ and transferring them to the Cusp trap, where they are electron-cooled and compressed again. Then we remove the electrons,[37] leaving a plasma of $> 99\%$ $\bar{p}$ with the properties given in Table I.

We trap beta-decay e^+ from a ^{22}Na source using a First Point Scientific system.[38] Every 1.05 s we move the e^+ to another trap at lower pressure, repeating until about 10^7 e^+ are in the low-pressure trap. We successively collect and transfer several such bunches from the low-pressure trap to the Cusp trap. We purify the e^+ plasma (99.98% e^+) to reduce the plasma expansion heating caused by positive ion contamination[39] and compress it using the SDREVC technique,[25,40] which ensures 1%-level reproducibility of the plasma radius r_0 and number of particles N. Note that the systematic uncertainty in estimating *in situ* plasma properties (even rows of Table I) from measured values (odd rows) is greater than 1%. See the Appendix for more details.

In mixing experiments, we ramp the electrode voltages so that the electrostatic potential morphs linearly from "Start" to "End," as shown in Fig. 2(a). Then we ramp the potentials back to Start and separate the remaining particles. In most cases, we count the leftover $\bar{p}$ by releasing them downstream (Null dump)—they hit the wall and annihilate near the field null at $z = -0.12$ m—and we keep most of the e^+ for the next run, releasing 10% of them upstream to measure T. Otherwise we dump each plasma as a whole to the MCP, one after the other, as quickly as possible so that the instabilities described in Sec. IV do not distort the density profiles, which we will present first in Sec. III.

III. TRENDS DURING MIXING

Figure 3(a) is a series of z-integrated density profiles obtained by interrupting the slow voltage ramp at different times during mixing and rapidly releasing plasma particles to the MCP. The plasma radius r_0 in Table I is derived from the profiles recorded at the start ($t = 0$). During mixing, the $\bar{p}$ in the upstream (US) well expand, and some are captured at low radius in the downstream (DS) well. The e^+ plasma does not expand measurably in this time.

Panel (b) complements (a) by quantifying the loss of $\bar{p}$ from the US well, the accumulation of $\bar{p}$ in the DS well, and the roughly constant number of e^+. The fraction f is the number of particles found in the corresponding well when mixing is interrupted, divided by the number of particles in the trap at the start of mixing. For $\bar{p}$, we calculate f using Fast Scintillator data, and for e^+, we use their space charge potential ϕ_e (see below). The drop in f causes the $\bar{p}$ plasma to expand, with density predicted to fall as f^2.[41] Using the central image intensity from panel (a) as a proxy for the plasma density, we find that the density falls slightly faster than f^2. [Lines fit to the first 35 s of data have slopes $(-1.7 \pm 0.07)\,\%\,s^{-1}$ for f^2 and $(-2.0 \pm 0.04)\,\%\,s^{-1}$ for the normalized image intensity.] This suggests a small amount of expansion from other sources. For $\bar{p}$, the nested well has the form of a "squeeze

TABLE I. Plasma properties: number of particles (N), radius (r_0), temperature (T), density (ρ), and Debye length (λ_D). The roman numerals refer to the corresponding section in this article. The e^+ plasma properties are averaged over the 50 to 60 s mixing duration, while the $\bar{p}$ ones are given only for the first 5 s of mixing, as they change significantly in time. Results from a numerical solver appear below each line of measured values. Measured values (odd rows) are accompanied by statistical uncertainties, and solver values (even rows) by systematic uncertainties. See the Appendix.

Species	Section	N (10^6)	r_0 (mm)	T (K)	ρ (10^8 cm^{-3})	λ_D (mm)
e^+	III	101 ± 2	1.50 ± 0.01	50 ± 20	···	···
		100 ± 10	1.4 ± 0.2	50 ± 20	2.0 ± 0.5	0.036 ± 0.009
	V	64 ± 1	1.26 ± 0.02	50 ± 20	···	···
		64 ± 9	1.3 ± 0.2	50 ± 20	1.5 ± 0.4	0.041 ± 0.009
$\bar{p}$	III	2.89 ± 0.04	1.14 ± 0.04	1700 ± 200	···	···
		2.9 ± 0.3	1.13 ± 0.07	1700 ± 200	0.80 ± 0.10	0.32 ± 0.02
	V	1.7 ± 0.1	1.07 ± 0.06	700 ± 100	···	···
		1.7 ± 0.2	1.05 ± 0.06	700 ± 100	0.46 ± 0.05	0.27 ± 0.03

26 October 2026 11:25:02

© Author(s) 2026

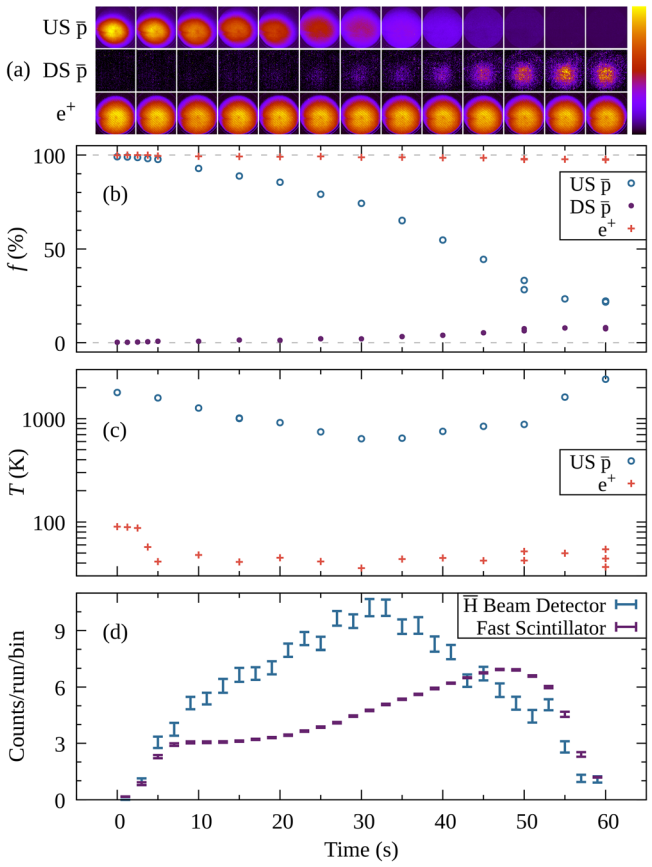


FIG. 3. Plasma diagnosed partway through mixing: (a) images, (b) fraction remaining f, (c) plasma temperature T, and (d) count rate at the $\overline{\mathrm{H}}$ beam detector and 1/1000 times the count rate at the Fast Scintillator. In (a), the side-length of the image squares is 4 cm, or about 5 mm in the trap (see the Appendix). The intensity scale is the same for all images in a given row. The color gradient corresponding to normalized intensity range 0–1 is given at the right of the image squares. The signals in (d) are the averages from 81 uninterrupted runs, with the standard deviation over these runs given as the error bars.

potential," which is known to enhance wave damping, transport, and heating, and can even reverse the net rotation of the plasma.[42–45]

Panel 3(c) shows T, which is measured with the MCP and SiPM as in Ref. 29. We measure T0.2 s after the end of the mixing ramp so that the e^+ do not have time to cool before being diagnosed. The $\overline{\mathrm{p}}$ temperature T_{p} falls during the first 30 s of mixing, then rises. The e^+ temperature T_{e} jumps to 100 K for the first few seconds, then falls and stays at (44 ± 5) K, which is also the steady state temperature with no $\overline{\mathrm{p}}$ in the trap.

The count rate at the $\overline{\mathrm{H}}$ Beam Detector, shown in panel (d), peaks when T_{p} reaches its minimum value. The Fast Scintillator count rate rises toward the end of mixing, indicating a higher rate of $\overline{\mathrm{p}}$ entering the e^+ plasma. The data comes from uninterrupted mixing runs in which a field ionizer partially blocks weakly bound atoms—those with less than about $k_{\mathrm{B}} \times 200$ K of binding energy, where k_{B} is Boltzmann's constant.[21]

We estimate changes in N as $\Delta N/N = \Delta f/f(t=0)$, where N (N_{e} and N_{p} for e^+ and $\overline{\mathrm{p}}$) is determined via separate measurements and verified numerically as described in the Appendix. We find that $|\Delta N_{\mathrm{e}}| = (2.9 \pm 0.3) \times 10^6$ e^+ and $|\Delta N_{\mathrm{p}}| = (2.3 \pm 0.2) \times 10^6 \overline{\mathrm{p}}$ leave the plasma during mixing. The $\overline{\mathrm{H}}$ yield is $|\Delta N_{\mathrm{p}}|$ as bare $\overline{\mathrm{p}}$ cannot escape the confining potentials in the mixing region. $|\Delta N_{\mathrm{e}}| - |\Delta N_{\mathrm{p}}| = 0.6 \times 10^6$ e^+ pass through the $\overline{\mathrm{p}}$ plasma and hit the MCP instead of forming $\overline{\mathrm{H}}$. We will show in Sec. V that these escaping e^+ reduce the $\overline{\mathrm{H}}$ yield by lowering $|\Delta N_{\mathrm{p}}|$.

IV. ANALOGY WITH SLOW EXTRACTION

We now present a $\overline{\mathrm{p}}$-only study that will help to understand some of the trends found in Sec. III. The same $\overline{\mathrm{p}}$ plasma is used, with the difference that no e^+ are loaded into the trap. We will use the term slow extraction for particles released gradually from the plasma, whether or not they escape the trap.

The radius r at which $\overline{\mathrm{p}}$ enter the e^+ plasma affects the velocity and binding energy of the $\overline{\mathrm{H}}$ formed.[46,47] The electric field $\mathbf{E}$ of the e^+ causes all charged particles in the plasma, including the $\overline{\mathrm{p}}$, to rotate with local velocity $\mathbf{E} \times \mathbf{B}/B^2$. In a constant-density plasma, $\mathbf{E}$ is proportional to r. As illustrated in Fig. 4, atoms formed at lower r drift outward more slowly and take longer to reach the radial edge of the plasma. This increases the binding energy (on average) because collisions with e^+ in the plasma tend to deexcite atoms once they have passed the kinetic bottleneck (a few times $k_{\mathrm{B}}T$ of binding energy).[16,48] Because these atoms also have lower transverse velocity, more of them escape the trap axially as a beam.

No model predicts the distribution of r for the $\overline{\mathrm{p}}$ in our case. At first, particles escape within $r < 2\lambda_{\mathrm{D}}$, where $\lambda_{\mathrm{D}} = \sqrt{\epsilon_0 k_{\mathrm{B}} T/\rho e^2}$ is the Debye length, ϵ_0 is the permittivity of free space, ρ is the plasma density, and e is the elementary charge.[49,50] This follows from Gauss's law for a thermal distribution of charges in the limit that only a small fraction of the plasma has been extracted. It does not apply to the majority

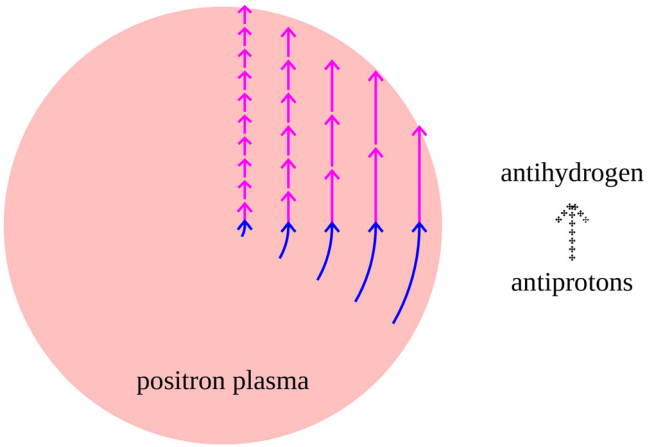


FIG. 4. Simple geometric model of $\overline{\mathrm{p}}$ and $\overline{\mathrm{H}}$ trajectories in the e^+ plasma. Thermal motion and cyclotron oscillations are not included. The plasma is cut in the plane perpendicular to $\mathbf{B}$. Each arrow represents one time step for a $\overline{\mathrm{p}}$ (blue) or $\overline{\mathrm{H}}$ (magenta). The atom is formed after the end of the first time step at $r = 0.1, 0.3, 0.5, 0.7$, or 0.9 times the e^+ radius and has speed (arrow length) proportional to r. The innermost trajectory is in the plasma ten times longer and emerges with nine times less transverse velocity. Such atoms are, on average, more deeply bound (more collisional deexcitation) and more likely to escape the trap axially (lower transverse velocity).

26 October 2026 11:25:02

© Author(s) 2026

of our $\overline{p}$: by definition, a plasma is many λ_D thick, and even before the inner Debye cylinder is emptied, the hollowing of the plasma makes it unstable.[51] The diocotron instability radically changes the plasma density profile and is not *a priori* predictable.[52]

We can directly measure r for $\overline{p}$ escaping the plasma in a situation analogous to mixing. Instead of releasing the $\overline{p}$ into the e^+, we release them toward the MCP. This does not include effects from ϕ_e or rebounding $\overline{p}$, which are present during mixing. Nevertheless, we will use this analogy to identify controllable behavior which seems generalizable and important to the case of mixing.

Figure 5 shows the spatial and temporal $\overline{p}$ profiles measured during slow extraction. The $\overline{p}$ are released to the MCP by removing the upstream barrier in a time τ, which we vary between 1 and 256 s. A linear ramp of the voltage applied to the barrier electrode results in a nonlinear change in well depth vs time. This means that the rate at which particles escape, shown in panel (b), would not be constant even if the particles were evenly distributed in energy and fixed at $r = 0$. In fact, kinetic energy and r also depend on time due to evaporative cooling and the growth of diocotron modes.[41,53] The escape rate vs time has a peak that shifts toward later times as τ is increased. For $\tau \geq 64$ s, the shape in (b) broadly matches the shape of Fast Scintillator count rate vs time for mixing, shown in Fig. 3(d).

We record videos[54] of the phosphor screen during extraction using a CMOS camera (Thorcam CS165MU1) exposed 50 ms per frame with about 5 ms dead time. The profiles shown in Fig. 5(a) are frame sums for the entire extraction. The videos show that the average radius of extracted particles decreases in time, reaching a minimum

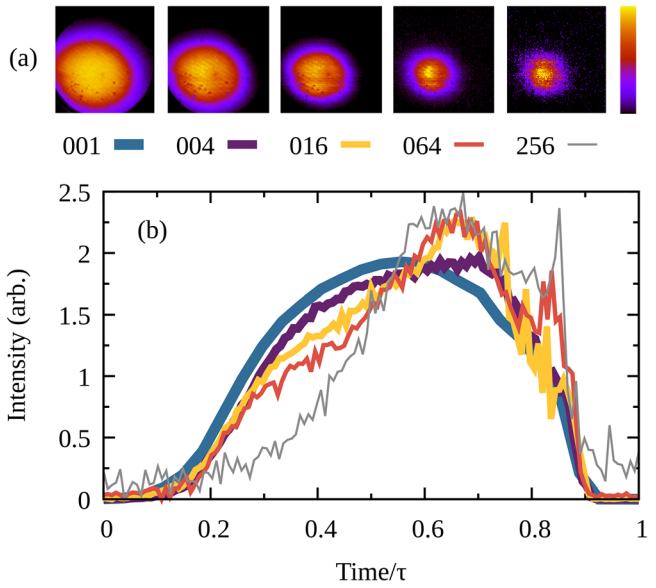


FIG. 5. Slow extraction of $\overline{p}$ to the MCP. (a) Transverse profiles integrated in time: each pixel is summed over all the frames of the corresponding video. Each image is then normalized to its own maximum. (b) Temporal profiles integrated in space: intensity is the sum of all pixel values in that frame. The intensity of each trace in (b) is normalized to its integral, and the time axis is rescaled such that 0 is the start of the extraction and 1 is the time τ (in seconds) given in the key under each image. The color gradient bar and the side-length of the image squares in (a) are the same as in Fig. 3.

when roughly half of the particles have escaped. Afterwards more violent instabilities develop, sometimes ejecting particles at $r \gg \lambda_D$.

On average, r is lower for slower extraction. Extracting slowly gives particles more time to refill the depleted center. The refilling rate could be proportional to the growth rate of the fastest-growing diocotron mode. For sufficiently slow extraction we expect $r < 2\lambda_D$. Note that λ_D increases as particles escape and ρ falls. Using a numerical solver (see the Appendix), we estimate $\lambda_D = (0.32 \pm 0.03)$ mm at the start of mixing (Sec. III).

The relation $r < 2\lambda_D$ might explain why the count rate at the $\overline{H}$ beam detector in Fig. 3(d) peaks when T_p is minimum. Using T_p from Fig. 3(c), and estimating relative changes in ρ via the central image intensity in Fig. 3(a), we find that λ_D is indeed falling for the first 30 s of mixing, albeit only by about 20%. Thus, the $\overline{H}$ beam detector signal is monotonically increasing in $1/\lambda_D$. On the other hand, some of the videos show an intense, low r feature forming late in the extraction, which we cannot link to T_p so easily. Either way, it is clear why the $\overline{p}$ in the DS well, shown in Fig. 3(a), have lower average radius than the ones in the US well. The DS well collects $\overline{p}$ extracted from the US well, most of which escape at $r < 2\lambda_D$. The DS image series may be the best indication of the actual $\overline{p}$ extraction radius during mixing.

The results of the $\overline{p}$-only experiments can be applied to $\overline{H}$ production. During mixing, the $\overline{p}$ plasma is simply a source of $\overline{p}$, most of which escape as $\overline{H}$ after bouncing a few thousand times through the e^+ plasma.[16] Thus, changing the total mixing duration is analogous to changing the extraction time, and we expect that only sufficiently slow mixing will correspond to $r < 2\lambda_D$.

Before describing the mixing experiments, we consider how this analogy can break down.

1. In slow extraction, if a $\overline{p}$ leaves the plasma, it does not return. In mixing, the $\overline{p}$ passes through a "squeeze" potential and a e^+ plasma. It returns with modified kinetic energy and transverse coordinates. As mentioned in Sec. III, the expansion rate of the $\overline{p}$ plasma during mixing is not much greater than the expectation in the absence of these effects, so they are probably not significant for bulk transport during mixing.
2. The $r < 2\lambda_D$ prediction assumes that the barrier potential outside the plasma is the same for all r, which is true if the blocking electrode is long compared to its radius.[28] This assumption is not valid for extraction into a e^+ plasma, which generates an additional r-dependent potential. In the Appendix, we show that this reduces the prediction to $r < 2\lambda_D\sqrt{\rho_p/\rho_e}$, where ρ_p (ρ_e) is the density at the center of the $\overline{p}$ (e^+) plasma.
3. Changing the mixing duration can change T_e and hence other properties that depend on it. We attempt to isolate that effect in the studies that we report next.

V. MIXING DURATION AND POSITRON HEATING

We now return to slow-merge mixing and vary the mixing duration, that is, the time from Start to End in Fig. 2(a), which we call τ in analogy with the extraction duration of Sec. IV. We use fewer particles for these experiments than in Sec. III: $1.7 \times 10^6 \overline{p}$ and 6.4×10^7 e^+, and mixing potentials that are similar but proportionately smaller.

Figure 6(a) shows how τ affects $\overline{H}$ production. The $\overline{H}$ per $\overline{p}$ efficiency ε, measured with the fast scintillator (see the Appendix), increases with τ in roughly the same way as the number of atoms

26 October 2026 11:25:02

© Author(s) 2026

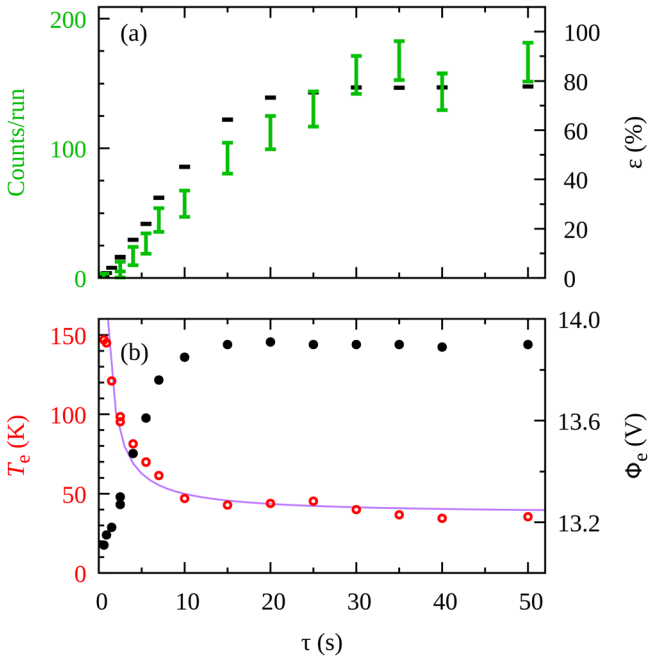


FIG. 6. Mixing for a variable duration τ. (a) $\overline{\text{H}}$ Beam Detector counts (green) and $\overline{\text{H}}$ formation efficiency ε (black). Background β is subtracted from each point using the formula $\beta = \beta_0 + \beta_{80} \cdot \varepsilon/80\%$, where β_0 is the number of counts per run in an equivalent window without $\bar{\text{p}}$ annihilations and β_{80} is the number when $\varepsilon = 80\%$ and the gate valve is closed so that no $\overline{\text{H}}$ can reach the $\overline{\text{H}}$ beam detector. Error bars in (a) are statistical, i.e., $\sqrt{\text{Counts/run}}$ or the equivalent for the ratio of Fast Scintillator counts that defines ε. This does not include uncertainty on the detection efficiency, which is used to calculate ε (see the Appendix). (b) e^+ plasma temperature T_e (red, open circles) and space charge ϕ_e (black, filled circles). The purple curve is Eq. (1) with $U_p = k_B \times 4000\,\text{K}$.

counted by the $\overline{\text{H}}$ beam detector. While ε saturates around 77% for $\tau \geq 30\,\text{s}$, the number of atoms in the beam may continue to increase with greater values of τ.

Figure 6(b) shows how τ affects the properties of the e^+ plasma, which we measure at the end of mixing. (For reference, the value of ϕ_e before mixing is 14.9 V.) Lower τ makes the plasma hotter because, in this time, the e^+ plasma absorbs kinetic energy from each $\bar{\text{p}}$ that enters and binding energy from each $\overline{\text{H}}$ that leaves. Call the sum of these energies U_p. The heating rate is approximately $U_p|\Delta N_p|/\tau$. The rate at which energy is lost is approximately $N_e k_B (T_e - T_0)/t_c$, where $t_c \approx 1.2\,\text{s}$ is the cyclotron cooling time at $z = -0.22\,\text{m}$ and $T_0 = (37 \pm 4)\,\text{K}$ is the equilibrium plasma temperature with no heating.[39] If we equate the heating and cooling rates, we get

$$k_B T_e = k_B T_0 + U_p \frac{t_c}{\tau} \frac{|\Delta N_p|}{N_e}, \tag{1}$$

which is plotted in the figure. The agreement with the data is best for $U_p \approx k_B \times 4000\,\text{K}$, which is much higher than the typical $\bar{\text{p}}$ thermal energy ($k_B \times 700\,\text{K}$) and binding energy ($k_B \times 200\,\text{K}$).[21] The $\bar{\text{p}}$ may gain extra kinetic energy as follows. When τ is short, there is insufficient time to refill the radial center of the $\bar{\text{p}}$ plasma, and $\bar{\text{p}}$ swept through the center by the diocotron instability can enter the e^+ plasma down a large potential drop. In the Appendix, we use the numerical solver to estimate a drop of $0.22\,\text{V} \approx k_B \times 2600\,\text{K/e}$ from $r = 0$ to $r = 2\lambda_D$. This explanation is only consistent if we assume that most of the τ values plotted are too short to achieve the reduced r mentioned in Point 2 at the end of Sec. IV.

Minimizing T_e is (at a microscopic level) the most important factor for optimizing the fraction of ground-state $\overline{\text{H}}$ atoms.[17] Equation (1) shows that, if T_e is to remain as low as possible, then a larger number of $\bar{\text{p}}$ (ΔN_p) requires either more mixing time (τ) or more e^+ (N_e).

To isolate the effect of T_e on the other variables, we fix $\tau = 50\,\text{s}$ and heat the plasma using white noise. We vary the noise power P on an azimuthally sectored electrode at $z = -0.17\,\text{m}$ (0.02 m downstream of the DS well). The noise is fed directly to two adjacent petals and phase shifted by 180° on the other two, so that each random Fourier component produces a dipole field. This only heats the e^+ (not the $\bar{\text{p}}$) in the range of P considered (see the Appendix). Figure 7 shows the results. T_e rises with increasing P, while $\overline{\text{H}}$ beam detector counts, ε, and ϕ_e fall.

Comparing the two figures, we find that ε falls by 50% for $T_e \approx 60\,\text{K}$ in Fig. 6, vs $T_e > 100\,\text{K}$ in Fig. 7. This shows that the increase in T_e for $\tau \to 0$ is only part of the cause for the drop in $\overline{\text{H}}$ production. The remainder could be attributed to the mechanisms discussed in Sec. IV.

T_e and ϕ_e are strongly anticorrelated in our data. Removing e^+ from the plasma reduces ϕ_e, and higher T_e means more e^+ leave the plasma during mixing. To see why, define the total confinement C as the difference between the local maximum of the confining potential at $z = -0.275\,\text{m}$ and the local minimum at $z = -0.23\,\text{m}$. It must be that $\phi_e - \phi_p < C$. As C is reduced during mixing, particles leave the

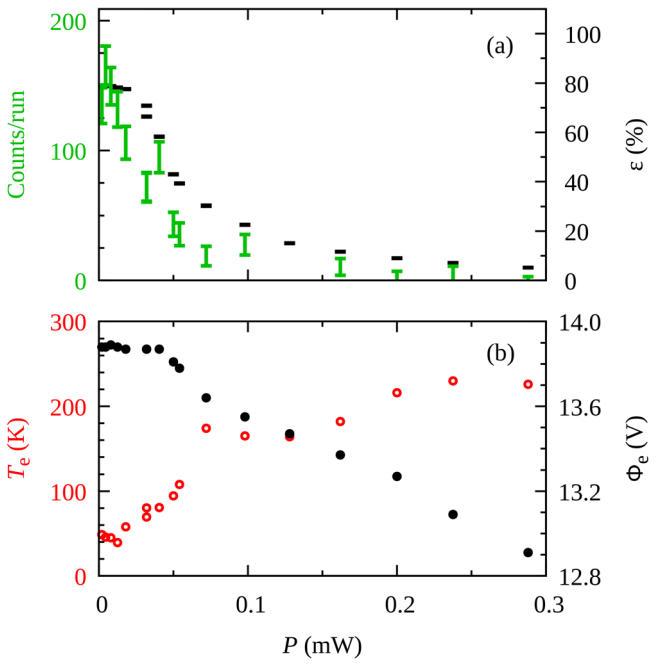


FIG. 7. Mixing while heating the e^+ with variable noise power P. (a) and (b) Error bars and background subtraction are the same as in Fig. 6. P is the mean-squared noise voltage applied to the electrode divided by 50 Ω, the value of the termination resistor at the vacuum feedthrough.

26 October 2026 11:25:02

© Author(s) 2026

plasma, lowering $\phi_e - \phi_p$. Whichever plasma is hotter will provide most of this difference, since collisions typically provide $k_B T$ of energy to escape the well. As T_e increases, more e^+ escape upstream and are wasted, which lowers ε because more $\bar{p}$ are left in the US well at the end of mixing. Note that higher T_e also reduces ε because of the T dependence of the 3-body recombination rate.[48] For maximum ε, the e^+ must be much colder than the $\bar{p}$. How much colder depends on other factors like the self-collision rate and the rate at which the center of each plasma is refilled.

VI. CONCLUSION

We demonstrate high efficiency antihydrogen production for slow-merge mixing of pure antiproton and positron plasmas, with 70% to 80% of the antiprotons forming stable antihydrogen. Relative to the previous state of the art,[20] we use 30 (50) times more antiprotons (positrons) and combine them in a 60 times longer period. Longer mixing time (i) favors antihydrogen formation at lower radius, which tends to reduce the transverse velocity and increase the binding energy; (ii) prevents unnecessary positron loss, thereby increasing the number of antiprotons that enter the positron plasma; and (iii) allows passive cyclotron radiation to keep the positrons cold as they absorb kinetic energy from the antiprotons and binding energy from the antihydrogen. These factors become increasingly important as we increase the number of antiprotons in the plasma, which is a common goal among groups that study antihydrogen.[9] (Very recently, the ALPHA collaboration increased their antihydrogen production rate by a factor of 4 relative to Ref. 20. One of the changes they reported was to increase the mixing time from "about 1 s" to "2 − 3 s," although the reason for this change was not stated.[55])

We provide experimental evidence linking the radius at which antiprotons enter the positron plasma to the amount of beam-like antihydrogen atoms produced in slow-merge mixing. We present slow extraction as a tool to study and potentially optimize that radius. This has led to a significant increase in the number of atoms leaving the trap as a beam.[18,21] The first in-beam measurement of the ground-state hyperfine splitting of antihydrogen may already be possible with the beam intensity we achieve in the experiments presented here.[56] The spectroscopy apparatus may require further reduction of beam velocity and increased binding energy, which can be achieved by lowering the antiproton plasma temperature. The present work shows that this temperature must, however, be much greater than the positron plasma temperature for efficient antihydrogen production.

Alternative methods, involving a spatially separated antiproton plasma or a traveling optical lattice, could vastly increase the fraction of atoms leaving the trap as a beam.[47,57] In the present method, the antiproton axial energy distribution is populated by collisions in the antiproton plasma, hence approximately thermal. It is impossible to obtain a mono-energetic beam this way. Cooling the antiprotons to lower temperature does not solve this problem, and our work suggests that such cooling may reduce the fraction of antiprotons that form antihydrogen. In the alternative methods, antiproton cooling reduces the energy spread without changing the mean energy of the beam, and, at least for Ref. 47, would not reduce the antihydrogen production efficiency. These methods can also be used for pulsed formation or extraction. In that case, ASACUSA could use the time of annihilation at the $\overline{H}$ beam detector to find each atom's velocity, which is valuable for our planned spectroscopy measurements. Rejecting fast atoms increases the signal-to-noise ratio, and knowing how long each atom is in the microwave cavity allows more accurate calculation of the spin-flip probability.

ACKNOWLEDGMENTS

We thank Andrew Christensen for sharing his numerical plasma solver, and the AD team for providing exceptionally stable and reliable beam at more than twice the design intensity. This work was supported by CERN, the Istituto Nazionale di Fisica Nucleare (INFN); the Japan Society for the Promotion of Science (JSPS) KAKENHI Grants Nos. 19KK0075, 20H01930, and 20KK0305; the Austrian Science Fund (FWF), Grants Nos. P 32468 and W1252-N27; the Deutsche Forschungsgemeinschaft (DFG); and the Royal Society.

AUTHOR DECLARATIONS

Conflict of Interest

The authors have no conflicts to disclose.

Author Contributions

E. D. Hunter: Writing – review & editing (equal). **M. Bumbar:** Writing – review & editing (equal). **C. Amsler:** Writing – review & editing (equal). **M. Bayo:** Writing – review & editing (equal). **H. Breuker:** Writing – review & editing (equal). **M. Cerwenka:** Writing – review & editing (equal). **G. Costantini:** Writing – review & editing (equal). **R. Ferragut:** Writing – review & editing (equal). **M. Giammarchi:** Writing – review & editing (equal). **A. Gligorova:** Writing – review & editing (equal). **G. Gosta:** Writing – review & editing (equal). **M. Hori:** Writing – review & editing (equal). **C. Killian:** Writing – review & editing (equal). **V. Kraxberger:** Writing – review & editing (equal). **N. Kuroda:** Writing – review & editing (equal). **A. Lanz:** Writing – review & editing (equal). **M. Leali:** Writing – review & editing (equal). **G. Maero:** Writing – review & editing (equal). **C. Malbrunot:** Writing – review & editing (equal). **V. Mascagna:** Writing – review & editing (equal). **Y. Matsuda:** Writing – review & editing (equal). **S. Migliorati:** Writing – review & editing (equal). **D. J. Murtagh:** Writing – review & editing (equal). **M. Romé:** Writing – review & editing (equal). **R. E. Sheldon:** Writing – review & editing (equal). **M. C. Simon:** Writing – review & editing (equal). **M. Tajima:** Writing – review & editing (equal). **V. Toso:** Writing – review & editing (equal). **S. Ulmer:** Writing – review & editing (equal). **L. Venturelli:** Writing – review & editing (equal). **A. Weiser:** Writing – review & editing (equal). **E. Widmann:** Writing – review & editing (equal).

DATA AVAILABILITY

The data that support the findings of this study are openly available in Zenodo at 10.5281/zenodo.17434838, Ref. 54.

APPENDIX: ANALYSIS OF PLASMA PROPERTIES

Here, we describe the models and approximations used to infer certain properties of the plasma. We first discuss the measurements from which we derive N_p, f, r_0, and ϕ_p, then we describe the numerical solver used to validate the measurements. We conclude with a treatment of statistical uncertainties.

26 October 2026 11:25:02

© Author(s) 2026

1. Measurements

We count $\bar{p}$ using the SiPM and MCP.[30,31] The standard charge pickoff method using a Faraday cup cannot be applied to count $\bar{p}$ because the charge collected (much more than 1 elementary charge per $\bar{p}$) includes unknown contributions from annihilation products, nuclear fragments, and electrons. Instead, we will compare the experimentally observed plasma properties with self-consistent numerical solutions that satisfy the Poisson equation and Boltzmann relation in our trap.

We use the fast scintillator to find f in Fig. 3(b). The fast scintillator efficiency depends on where the $\bar{p}$ annihilate. We calibrate the fast scintillator empirically using data from the experiments described in Secs. III and V. The total number of $\bar{p}$ at the start of mixing (N_p) is constant and the number of $\overline{H}$ (N_H) depends on the time at which mixing is interrupted (Fig. 3), τ (Fig. 6), or P (Fig. 7). If the fast scintillator registers M counts at mixing and D counts at the null dump, we have

$$N_H + (N_p - N_H) = N_p, \tag{A1}$$

$$\frac{M}{a} + \frac{D}{b} = N_p, \tag{A2}$$

$$M\frac{b}{a} + D = \text{constant}, \tag{A3}$$

where a and b are the fast scintillator counting efficiency for mixing and null dump annihilations. The correct value of b/a in Eq. (A3) should yield the same number for all runs as N_H varies. The value $b/a = 1.41$ minimizes the standard deviation for the combined data series. To find the absolute values of a and b, we vary the number of $\bar{p}$, alternating mixing runs with runs where we use the SiPM to count the $\bar{p}$ (see companion article). We obtain $a^{-1} = 17$ and $b^{-1} = 12\bar{p}$ per Fast Scintillator count at mixing and null dump, respectively. Note that the contribution from e^+ annihilations is negligible.[39]

We extract r_0 from the measured density profile. We fit the profile to $A \cdot \exp[-(r/r_0)^n] + B$. A is an amplitude, B is a constant background, n controls how quickly the function decays, and r_0 represents the characteristic radius.[58] We then apply a magnification factor: $r_0 = r_{MCP}\sqrt{B_{MCP}/B_0}$, because magnetized particles follow the diverging field lines from trap (B_0) to MCP (B_{MCP}). For the same reason, we expect the plasma radius to vary inversely as $\sqrt{B}$ inside the trap.[59] That effect is small for the $\bar{p}$ ($\delta B/B \approx 5\%$), and is included in our uncertainties as explained below.

We measure ϕ simultaneously with T. The first particles detected should escape when the plasma is barely confined, so the confinement potential at that time is an estimate of ϕ. This overestimates the true value of ϕ by an amount proportional to T. The constant of proportionality should be a function of the detector sensitivity, the ramp rate, and the number of particles in the plasma.[39] We obtain the best estimate of ϕ by making a graph of measured ϕ vs T, with other properties constant. Figure 8(a) shows such a graph for $\bar{p}$ diagnosed using the same electrodes, voltage ramps, MCP bias, and analysis routines as we use for Fig. 3(c). The $\bar{p}$ are evaporatively cooled to fix ϕ_p (and to some extent N_p) at three different values, then heated in the DS well (see Sec. III) with $0.002 < P < 0.2$ mW (see Sec. V). The increase in T_p with P is much less for lower N_p, which incidentally corroborates our

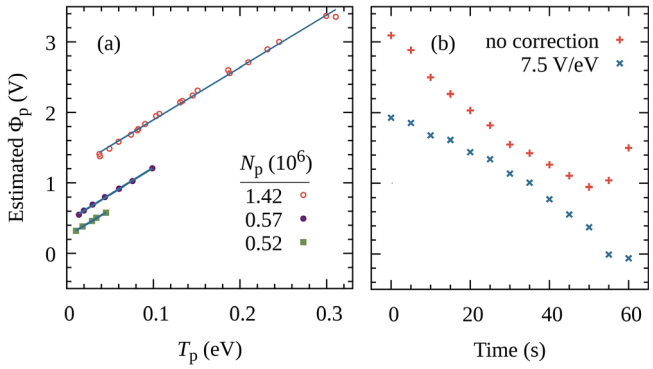


FIG. 8. Calibration and measurement of ϕ_p. (a) Dependence of measured ϕ_p on T_p. (b) Decay of ϕ_p during mixing. In (a), we use three different quantities of $\bar{p}$ (N_p). In (b), we show the data with and without the calibrated correction $d\phi_p/dT_p = 7.5$ V/eV from (a).

statement in Sec. V that this range of P does not heat the relatively small number of $\bar{p}$ in the DS well during mixing. The best-fit lines have slopes (7.4 ± 0.1), (7.6 ± 0.1), and (7.5 ± 0.2) V/eV. Figure 8(b) shows estimates of ϕ_p as a function of mixing time (Sec. III), with and without applying the calibration of panel (a). The calibration brings the data much closer to the measured f values shown in Fig. 3(b). It seems to slightly overcompensate for the last two points near $\phi_p = 0$, where the correction itself is much larger than the true value of ϕ_p.

2. Numerical solution

The numerical solver takes as input the electrode geometry, trap potentials, B, T, N, and plasma rotation rate ω_r.[60] It finds a solution with N charges distributed such that $\rho(r,z) = \rho_0 \exp[e(\Phi(r,z) - \Phi_0)/k_B T]$. Here, Φ is the total electrostatic potential due to both the voltages applied to the electrodes and the space charge of the plasma, and ρ_0 and Φ_0 are ρ and Φ evaluated at the center of the plasma.

We set the trap potentials to match the experimental conditions at the start of mixing and repeatedly solve for different values of ω_r. For a given T and N, this produces solutions with a range of r_0 values. We use these solutions for three things: First, to obtain ρ and λ_D, which we cannot derive from our measurements with simple formulas. Second, to verify that the properties we measure are self-consistent, i.e., correspond to a valid equilibrium state. Third, to gauge the amount of variation in the plasma properties that would still be consistent with our measurements, which we take as (an upper bound on) our systematic uncertainty.

Figure 9 shows example density profiles obtained using the numerical solver for the conditions reported in Sec. III. The measured radial profiles (using pixel intensity as a proxy for axially integrated density[32]) are consistent with the solver prediction for plasma properties in the ranges given in Table I. Note that the MCP is only sensitive to about $r < 2.5$ mm for $\bar{p}$ and $r < 2.2$ mm for e^+, given the different magnification factors for the two species (see Subsection 3 of the Appendix).

Figure 10 shows example potential contours in z for different values of r, now for the conditions reported in Sec. V. Consider the

26 October 2026 11:25:02

© Author(s) 2026

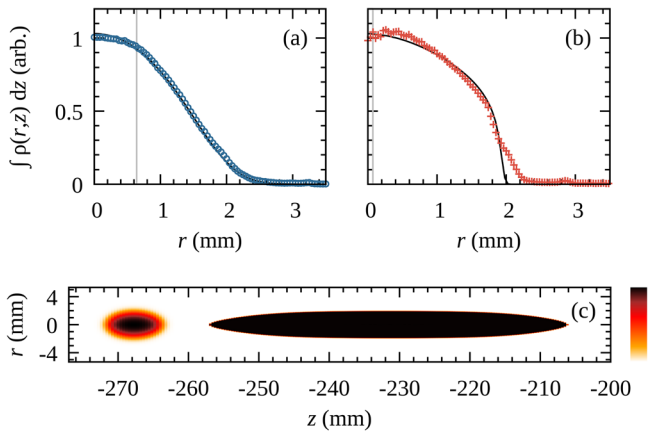


FIG. 9. Density profiles $\rho(r,z)$ at the start of mixing, with $\bar{p}$ on the left and e^+ on the right. (a) and (b) Density on an (axially integrated) radial slice through the plasma. Colored points are derived from measurements in Fig. 3(a), and black curves from the data in panel (c). The condition $r = 2\lambda_D$ is indicated by a vertical gray line. (c) 2D profiles obtained with the plasma solver. The color bar goes from 0 to the peak density, $\rho_0 = 6.0 \times 10^7$ cm^{-3} for the $\bar{p}$ and $\rho_0 = 2.5 \times 10^8$ cm^{-3} for the e^+.

curves starting inside the $\bar{p}$ plasma at $z = -0.266$ m and ending inside the e^+ plasma at $z = -0.253$ m. The potential drop along the curves at $r = 0$ and $r = 2\lambda_D$ differs by 0.22 V ($\lambda_D = 0.27$ mm is the $\bar{p}$ Debye length). This energy scale (per charge) is comparable to the U_p found using Eq. (1) to fit the data in Sec. V.

In an infinitely long cylindrical plasma, $\bar{p}$ at $r = 2\lambda_D$ see a potential difference of $2k_B T_p/e$ with respect to $r = 0$.[58] In the e^+ plasma, we get the same potential at a lower radius, $2\lambda_D\sqrt{\rho_p/\rho_e}$. This is because the potential scales as r^2 in an infinitely long plasma, and λ_D scales as $\rho^{1/2}$. We can check this using the numerical model. Using the data in Fig. 10, we find the r in the e^+ that corresponds to the same potential difference as from $r = 0$ to $r = 2\lambda_D$ in the $\bar{p}$ plasma. This is true for $r = 0.30$ mm, which matches the infinite length prediction exactly: $2\lambda_D\sqrt{\rho_p/\rho_e} = 0.30$ mm for Sec. V values in Table I.

3. Uncertainties

In Table I, we compile measured values of N, r_0, T, and numerical results for N, r_0, T, ρ, and λ_D. The statistical uncertainties for the measured values are the standard deviation in three or more repeated measurements of the same quantity. The systematic uncertainties, given with the numerical results, depend on the following factors:

N_p: The detection efficiency of the MCP-phosphor-photomultiplier system is unknown. The upper bound is 100%. The lower bound is taken as 93%, as obtained in Ref. 30. While we are not sure that those authors achieved high enough gain so that all events were above threshold, our measured amplitude distribution suggests that we do,[31] so our detection efficiency should be at least as great as theirs.

N_p: Pions, formed upon annihilation when $\bar{p}$ hit the copper mesh at $z = -0.5$ m, may reach the MCP and emulate a $\bar{p}$ signal. As the MCP is 0.4 m from the mesh and has a diameter 0.04 m, the relative solid angle is less than 1%. We estimate that charged pions (typically two or four per $\bar{p}$) coming from the 21% of $\bar{p}$ that annihilate on the mesh contribute less than 1% of the signal.

N_e: Secondary electrons can leave the MCP when it is used as a Faraday Cup, causing us to overestimate the positive charge of the e^+ plasma. To characterize this effect, we vary the MCP-front bias between -100 and $+20$ V, measuring N_e simultaneously via the charge collected by the MCP and the light produced in a plastic scintillator outside the MCP chamber. The latter is proportional to the number of e^+ that hit the MCP. A bias of -7 V (or lower) maximizes the scintillator signal. However, a bias of $+25$ V is needed to retain most of the secondary electrons.[61,62] Comparing the data from scintillator and MCP at $+25$ and -7 V, we infer that the charge signal at -7 V bias is higher than true N_e by about 25%. As elsewhere, we split the difference in our lack of certainty, taking 87% of the measured value as the center and 13% of the measured value as the systematic uncertainty.

T: The plasma temperature diagnostic,[28] in its simplest form, assumes that ϕ is constant. In fact, ϕ decreases because of escaping charge and because the well gets longer as the confining potential is reduced, causing us to overestimate T.[60] The effect should be about 10% in our case, which is comparable to the statistical variation from run to run, and consistent with the (little or no) variation in T that we observe for electron plasma diagnosed from wells of different length.

r_0: The mirror ratio B_{MCP}/B_0 cannot be measured while the trap is in place. It is taken from field maps provided by the manufacturer, which we have verified (with the trap removed) at the 1% level.

r_0: The mirror-ratio prediction described above assumes that particles follow magnetic field lines exactly. That is an imperfect assumption, both inside the trap and between the trap and the

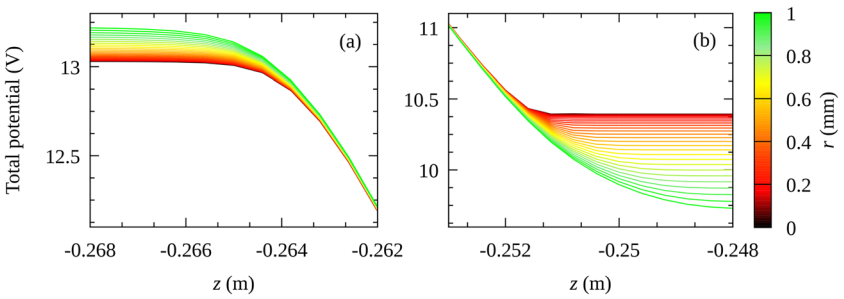


FIG. 10. Total electrostatic potential (trap plus plasma) at the start of mixing. Contours are drawn at fixed r as given by the color bar. (a) is near the downstream edge of the $\bar{p}$ plasma and (b) is near the upstream edge of the e^+ plasma.

26 October 2026 11:25:02

© Author(s) 2026

MCP. First, the plasma changes shape as it is carried about the trap through regions of varying B. When it is moved from the mixing potentials, at high B, to the dump-diagnosis well, at low B, the particles should not exactly follow magnetic field lines, because that would generate large potential gradients within the plasma.[59] Second, particles drift transversely across field lines whenever the electric field is perpendicular to B, as is the case near the MCP. We quantify this effect via the discrepancy between the mirror-ratio prediction and the inferred size of the copper mesh, which appears as a shadow when the plasma is extracted through it for imaging.[26] The discrepancy corresponds to a change in the inferred radius of about +30% for electrons, +25% for e^+, and −4% for $\bar{p}$. Thus, we obtain four predictions for the true r_0, depending on whether or not particles follow field lines within the trap and outside of the trap. We take the range of possible r_0 to be the mean of these predictions plus or minus their standard deviation.

λ_D: The numerical solver assumes that the plasma can be decomposed as a set of concentric cylindrical shells of different lengths. This neglects a possible cone-shaped distortion, which should arise because B varies in z.[59] The variation of B, and hence n, is at most 10% from one end of the plasma to the other. This contributes an additional 5% uncertainty to λ_D (and to r_0), which we compound with the standard deviation described below.

We use these uncertainties, combined in quadrature with the statistical uncertainties, to find ranges of acceptable N, T, and r_0, then find plasma solutions that evenly span those ranges (in r_0) or sit at extreme values (in N and T). The mean and standard deviation of this set of solutions are the numerical result and the systematic uncertainty for each variable given in Table I.

REFERENCES

[1]M. Aguilar, G. Ambrosi, H. Anderson, L. Arruda, N. Attig, C. Bagwell, F. Barao, M. Barbanera, L. Barrin, A. Bartoloni, R. Battiston, A. Bayyari, N. Belyaev, B. Bertucci, V. Bindi, K. Bollweg, J. Bolster, M. Borchiellini, B. Borgia, M. Boschini, M. Bourquin, C. Brugnoni, J. Burger, W. J. Burger, X. Cai, M. Capell, J. Casaus, G. Castellini, F. Cervelli, Y. Chang, G. Chen, G. Chen, H. Chen, H. Chen, Y. Chen, L. Cheng, H. Chou, S. Chouridou, V. Choutko, C. Chung, C. Clark, G. Coignet, C. Consolandi, A. Contin, C. Corti, Z. Cui, K. Dadzie, F. D'Angelo, A. Dass, C. Delgado, S. Della Torre, M. Demirköz, L. Derome, S. Di Falco, V. Di Felice, C. Díaz, F. Dimiccoli, P. von Doetinchem, F. Dong, M. Duranti, A. Egorov, A. Eline, F. Faldi, D. Fehr, J. Feng, E. Fiandrini, P. Fisher, V. Formato, R. García-López, C. Gargiulo, H. Gast, M. Gervasi, F. Giovacchini, D. Gómez-Coral, J. Gong, D. Grandi, M. Graziani, S. Haino, K. Han, R. Hashmani, Z. He, B. Heber, F. Hernández-Nicolás, T. Hsieh, J. Hu, B. Huang, M. Ionica, M. Incagli, Y. Jia, H. Jinchi, G. Karagöz, T. Kirn, A. Klipfel, O. Kounina, A. Kounine, V. Koutsenko, D. Krasnopevtsev, A. Kuhlman, A. Kulemzin, G. La Vacca, E. Laudi, G. Laurenti, G. LaVecchia, I. Lazzizzera, H. Lee, S. Lee, H. Li, J. Li, J. Li, M. Li, M. Li, Q. Li, Q. Li, Q. Li, S. Li, S. Li, Z. Li, M. Liang, P. Liao, C. Lin, T. Lippert, J. Liu, P. Liu, S. Lu, Y. Lu, J. Luo, Q. Luo, S. Luo, X. Luo, C. Mañá, J. Marín, J. Marquardt, G. Martínez, N. Masi, D. Maurin, T. Medvedeva, A. Menchaca-Rocha, Q. Meng, V. Mikhailov, M. Molero, P. Mott, L. Mussolin, Y. N. Jozani, R. Nicolaidis, N. Nikonov, F. Nozzoli, J. Ocampo-Peleteiro, A. Oliva, M. Orcinha, F. Palmonari, M. Paniccia, A. Pashnin, M. Pauluzzi, D. Pelosi, S. Pensotti, P. Pietzcker, V. Plyaskin, S. Poluianov, D. Pridöhl, Z. Qu, L. Quadrani, P. Rancoita, D. Rapin, A. R. Conde, E. Robyn, I. Rodríguez-García, L. Romaneehsen, F. Rossi, A. Rozhkov, D. Rozza, R. Sagdeev, S. Schael, A. S. von Dratzig, G. Schwering, E. Seo, B. Shan, A. Shukla, T. Siedenburg, G. Silvestre, J. Song, X. Song, R. Sonnabend, L. Strigari, T. Su, Q. Sun, Z. Sun, L. Tabarroni, M. Tacconi, Z. Tang, J. Tian, Y. Tian, S. C. Ting, S. Ting, N. Tomassetti, J. Torsti, A. Ubaldi, T. Urban, I. Usoskin, V. Vagelli, R. Vainio, P. Väisänen, M. Valencia-Otero, E. Valente, E. Valtonen, M. V. Acosta, M. Vecchi, M. Velasco, C. Wang, J. Wang, L. Wang, L. Wang, N. Wang, Q. Wang, S. Wang, X. Wang, Z. Wang, J. Wei, Z. Weng, H. Wu, Y. Wu, Z. Wu, J. Xiao, R. Xiong, X. Xiong, W. Xu, Q. Yan, H. Yang, Y. Yang, H. Yi, Y. You, Y. Yu, Z. Yu, C. Zhang, F. Zhang, J. Zhang, J. Zhang, Z. Zhang, P. Zhao, C. Zheng, Z. Zheng, H. Zhuang, V. Zhukov, A. Zichichi, M. Zuberi, and P. Zuccon, "Antiprotons and elementary particles over a solar cycle: Results from the alpha magnetic spectrometer," Phys. Rev. Lett. **134**, 051002 (2025).

[2]N. Kuroda, H. A. Torii, Y. Nagata, M. Shibata, Y. Enomoto, H. Imao, Y. Kanai, M. Hori, H. Saitoh, H. Higaki, A. Mohri, K. Fujii, C. H. Kim, Y. Matsuda, K. Michishio, Y. Nagashima, M. Ohtsuka, K. Tanaka, and Y. Yamazaki, "Development of a monoenergetic ultraslow antiproton beam source for high-precision investigation," Phys. Rev. Accel. Beams **15**, 024702 (2012).

[3]P. Blumer, M. Charlton, M. Chung, P. Clade, P. Comini, P. Crivelli, O. Dalkarov, P. Debu, L. Dodd, A. Douillet *et al.*, "Positron accumulation in the GBAR experiment," Nucl. Instrum. Methods Phys. Res., Sect. A **1040**, 167263 (2022).

[4]J. H. Malmberg and J. S. deGrassie, "Properties of nonneutral plasma," Phys. Rev. Lett. **35**, 577–580 (1975).

[5]S. Maury, "The antiproton decelerator: AD," Hyperfine Interact. **109**, 43–52 (1997).

[6]M. Hori and J. Walz, "Physics at CERN's antiproton decelerator," Prog. Part. Nucl. Phys. **72**, 206–253 (2013).

[7]C. Amole, M. D. Ashkezari, M. Baquero-Ruiz, W. Bertsche, E. Butler, A. Capra, C. L. Cesar, M. Charlton, S. Eriksson, J. Fajans, T. Friesen, M. C. Fujiwara, D. R. Gill, A. Gutierrez, J. S. Hangst, W. N. Hardy, M. E. Hayden, C. A. Isaac, S. Jonsell, L. Kurchaninov, A. Little, N. Madsen, J. T. K. McKenna, S. Menary, S. C. Napoli, P. Nolan, K. Olchanski, A. Olin, A. Povilus, P. Pusa, C. O. Rasmussen, F. Robicheaux, E. Sarid, D. M. Silveira, C. So, T. D. Tharp, R. I. Thompson, D. P. van der Werf, Z. Vendeiro, J. S. Wurtele, A. I. Zhmoginov, and A. E. Charman, "An experimental limit on the charge of antihydrogen," Nat. Commun. **5**, 3955 (2014).

[8]G. B. Andresen, M. D. Ashkezari, M. Baquero-Ruiz, W. Bertsche, P. D. Bowe, E. Butler, C. L. Cesar, M. Charlton, A. Deller *et al.*, "Confinement of antihydrogen for 1,000 seconds," Nat. Phys. **7**, 558–564 (2011).

[9]W. A. Bertsche, E. Butler, M. Charlton, and N. Madsen, "Physics with antihydrogen," J. Phys. B **48**, 232001 (2015).

[10]E. K. Anderson, C. J. Baker, W. Bertsche, N. M. Bhatt, G. Bonomi, A. Capra, I. Carli, C. L. Cesar, M. Charlton, A. Christensen, R. Collister, A. Cridland Mathad, D. Duque Quiceno, S. Eriksson, A. Evans, N. Evetts, S. Fabbri, J. Fajans, A. Ferwerda, T. Friesen, M. C. Fujiwara, D. R. Gill, L. M. Golino, M. B. Gomes Gonçalves, P. Grandemange, P. Granum, J. S. Hangst, M. E. Hayden, D. Hodgkinson, E. D. Hunter, C. A. Isaac, A. J. U. Jimenez, M. A. Johnson, J. M. Jones, S. A. Jones, S. Jonsell, A. Khramov, N. Madsen, L. Martin, N. Massacret, D. Maxwell, J. T. K. McKenna, S. Menary, T. Momose, M. Mostamand, P. S. Mullan, J. Nauta, K. Olchanski, A. N. Oliveira, J. Peszka, A. Powell, C. O. Rasmussen, F. Robicheaux, R. L. Sacramento, M. Sameed, E. Sarid, J. Schoonwater, D. M. Silveira, J. Singh, G. Smith, C. So, S. Stracka, G. Stutter, T. D. Tharp, K. A. Thompson, R. I. Thompson, E. Thorpe-Woods, C. Torkzaban, M. Urioni, P. Woosaree, and J. S. Wurtele, "Observation of the effect of gravity on the motion of antimatter," Nature **621**, 716–722 (2023).

[11]A. D. Sakharov, "Violation of CP Invariance, C asymmetry, and baryon asymmetry of the universe," Pisma Zh. Eksp. Teor. Fiz. **5**, 32–35 (1967).

[12]G. B. Andresen, M. D. Ashkezari, M. Baquero-Ruiz, W. Bertsche, P. D. Bowe, E. Butler, C. L. Cesar, S. Chapman, M. Charlton, A. Deller, S. Eriksson, J. Fajans, T. Friesen, M. C. Fujiwara, D. R. Gill, A. Gutierrez, J. S. Hangst, W. N. Hardy, M. E. Hayden, A. J. Humphries, R. Hydomako, M. J. Jenkins, S. Jonsell, L. V. Jørgensen, L. Kurchaninov, N. Madsen, S. Menary, P. Nolan, K. Olchanski, A. Olin, A. Povilus, P. Pusa, F. Robicheaux, E. Sarid, S. S. el Nasr, D. M. Silveira, C. So, J. W. Storey, R. I. Thompson, D. P. van der Werf, J. S. Wurtele, and Y. Yamazaki, "Trapped antihydrogen," Nature **468**, 673–676 (2010).

[13]G. Gabrielse, R. Kalra, W. S. Kolthammer, R. McConnell, P. Richerme, D. Grzonka, W. Oelert, T. Sefzick, M. Zielinski, D. W. Fitzakerley, M. C. George, E. A. Hessels, C. H. Storry, M. Weel, A. Müllers, and J. Walz, "Trapped antihydrogen in its ground state," Phys. Rev. Lett. **108**, 113002 (2012).

[14]E. Widmann, R. Hayano, M. Hori, and T. Yamazaki, "Measurement of the hyperfine structure of antihydrogen," Nucl. Instrum. Methods Phys. Res., Sect. B **214**, 31–34 (2004).

26 October 2026 11:25:02

© Author(s) 2026

[15]C. Malbrunot, M. Diermaier, M. Simon, C. Amsler, S. Arguedas Cuendis, H. Breuker, C. Evans, M. Fleck, B. Kolbinger, A. Lanz, M. Leali, V. Maeckel, V. Mascagna, O. Massiczek, Y. Matsuda, Y. Nagata, C. Sauerzopf, L. Venturelli, E. Widmann, M. Wiesinger, Y. Yamazaki, and J. Zmeskal, "A hydrogen beam to characterize the asacusa antihydrogen hyperfine spectrometer," Nucl. Instrum. Methods Phys. Res., Sect. A **935**, 110–120 (2019).
[16]F. Robicheaux, "Simulations of antihydrogen formation," Phys. Rev. A **70**, 022510 (2004).
[17]B. Radics, D. J. Murtagh, Y. Yamazaki, and F. Robicheaux, "Scaling behavior of the ground-state antihydrogen yield as a function of positron density and temperature from classical-trajectory monte carlo simulations," Phys. Rev. A **90**, 032704 (2014).
[18]B. Kolbinger, C. Amsler, S. A. Cuendis, H. Breuker, A. Capon, G. Costantini, P. Dupré, M. Fleck, A. Gligorova, H. Higaki, Y. Kanai, V. Kletzl, N. Kuroda, A. Lanz, M. Leali, V. Mäckel, C. Malbrunot, V. Mascagna, O. Massiczek, Y. Matsuda, D. J. Murtagh, Y. Nagata, A. Nanda, L. Nowak, B. Radics, C. Sauerzopf, M. C. Simon, M. Tajima, H. A. Torii, U. Uggerh Ø j, S. Ulmer, L. Venturelli, A. Weiser, M. Wiesinger, E. Widmann, T. Wolz, Y. Yamazaki, and J. Zmeskal, "Measurement of the principal quantum number distribution in a beam of antihydrogen atoms," Eur. Phys. J. D **75**, 91 (2021).
[19]G. Gabrielse, S. L. Rolston, L. Haarsma, and W. Kells, "Possible antihydrogen production using trapped plasmas," Hyperfine Interact. **44**, 287–293 (1989).
[20]M. Ahmadi, B. X. R. Alves, C. J. Baker, W. Bertsche, E. Butler, A. Capra, C. Carruth, C. L. Cesar, M. Charlton, S. Cohen, R. Collister, S. Eriksson, A. Evans, N. Evetts, J. Fajans, T. Friesen, M. C. Fujiwara, D. R. Gill, A. Gutierrez, J. S. Hangst, W. N. Hardy, M. E. Hayden, C. A. Isaac, A. Ishida, M. A. Johnson, S. A. Jones, S. Jonsell, L. Kurchaninov, N. Madsen, M. Mathers, D. Maxwell, J. T. K. McKenna, S. Menary, J. M. Michan, T. Momose, J. J. Munich, P. Nolan, K. Olchanski, A. Olin, P. Pusa, C. O. Rasmussen, F. Robicheaux, R. L. Sacramento, M. Sameed, E. Sarid, D. M. Silveira, S. Stracka, G. Stutter, C. So, T. D. Tharp, J. E. Thompson, R. I. Thompson, D. P. van der Werf, and J. S. Wurtele, "Antihydrogen accumulation for fundamental symmetry tests," Nat. Commun. **8**, 681 (2017).
[21]E. D. Hunter, M. Bumbar, C. Amsler, M. N. Bayo, H. Breuker, M. Cerwenka, G. Costantini, R. Ferragut, M. Giammarchi, A. Gligorova, G. Gosta, M. Hori, C. Killian, V. Kraxberger, N. Kuroda, A. Lanz, M. Leali, G. Maero, C. Malbrunot, V. Mascagna, Y. Matsuda, S. Migliorati, D. J. Murtagh, M. Romé, R. E. Sheldon, M. C. Simon, M. Tajima, V. Toso, S. Ulmer, L. Venturelli, A. Weiser, and E. Widmann, "Measured properties of an antihydrogen beam," arXiv:2509.02583 (2025).
[22]Y. Enomoto, N. Kuroda, K. Michishio, C. H. Kim, H. Higaki, Y. Nagata, Y. Kanai, H. A. Torii, M. Corradini, M. Leali, E. Lodi-Rizzini, V. Mascagna, L. Venturelli, N. Zurlo, K. Fujii, M. Ohtsuka, K. Tanaka, H. Imao, Y. Nagashima, Y. Matsuda, B. Juhász, A. Mohri, and Y. Yamazaki, "Synthesis of cold antihydrogen in a cusp trap," Phys. Rev. Lett. **105**, 243401 (2010).
[23]Y. Nagata and Y. Yamazaki, "A novel property of anti-helmholz coils for in-coil syntheses of antihydrogen atoms: Formation of a focused spin-polarized beam," New J. Phys. **16**, 083026 (2014).
[24]Y. Nagata, Y. Kanai, N. Kuroda, H. Higaki, Y. Matsuda, and Y. Yamazaki, "The development of the superconducting double cusp magnet for intense antihydrogen beams," J. Phys.: Conf. Ser. **635**, 022062 (2015).
[25]E. D. Hunter, C. Amsler, H. Breuker, M. Bumbar, S. Chesnevskaya, G. Costantini, R. Ferragut, M. Giammarchi, A. Gligorova, G. Gosta, H. Higaki, C. Killian, V. Kraxberger, N. Kuroda, A. Lanz, M. Leali, G. Maero, C. Malbrunot, V. Mascagna, Y. Matsuda, V. Mäckel, S. Migliorati, D. Murtagh, A. Nanda, L. Nowak, F. Parnefjord Gustafsson, S. Rheinfrank, M. Romé, M. Simon, M. Tajima, V. Toso, S. Ulmer, L. Venturelli, A. Weiser, E. Widmann, Y. Yamazaki, and J. Zmeskal, "SDR, EVC, and SDREVC: Limitations and extensions," J. Plasma Phys. **89**, 955890501 (2023).
[26]C. Amsler, H. Breuker, S. Chesnevskaya, G. Costantini, R. Ferragut, M. Giammarchi, A. Gligorova, G. Gosta, H. Higaki, E. D. Hunter, C. Killian, V. Kletzl, V. Kraxberger, N. Kuroda, A. Lanz, M. Leali, V. Mäckel, G. Maero, C. Malbrunot, V. Mascagna, Y. Matsuda, S. Migliorati, D. J. Murtagh, Y. Nagata, A. Nanda, L. Nowak, E. Pasino, M. Romé, M. C. Simon, M. Tajima, V. Toso, S. Ulmer, L. Venturelli, A. Weiser, E. Widmann, T. Wolz, Y. Yamazaki, and J. Zmeskal, "Reducing the background temperature for cyclotron cooling in a cryogenic penning–malmberg trap," Phys. Plasmas **29**, 083303 (2022).
[27]S. Sellner, M. Besirli, M. Bohman, M. J. Borchert, J. Harrington, T. Higuchi, A. Mooser, H. Nagahama, G. Schneider, C. Smorra, T. Tanaka, K. Blaum, Y. Matsuda, C. Ospelkaus, W. Quint, J. Walz, Y. Yamazaki, and S. Ulmer, "Improved limit on the directly measured antiproton lifetime," New J. Phys. **19**, 083023 (2017).
[28]D. L. Eggleston, C. F. Driscoll, B. R. Beck, A. W. Hyatt, and J. H. Malmberg, "Parallel energy analyzer for pure electron plasma devices," Phys. Fluids B **4**, 3432–3439 (1992).
[29]E. D. Hunter, J. Fajans, N. A. Lewis, A. P. Povilus, C. Sierra, C. So, and D. Zimmer, "Plasma temperature measurement with a silicon photomultiplier (SiPM)," Rev. Sci. Instrum. **91**, 103502 (2020).
[30]S. S. Frederiksen, "Counting anti-protons with an MCP-SiPM setup to determine the absolute number of anti-protons in the ALPHA experiment," Report No. CERN-STUDENTS-Note-2022-035 (CERN, 2022).
[31]M. G. Cripe, "Summer student project report: Counting antiprotons in ASACUSA's Cusp trap," Report No. CERN-STUDENTS-Note-2024-139 (CERN, 2024).
[32]G. B. Andresen, W. Bertsche, P. D. Bowe, C. C. Bray, E. Butler, C. L. Cesar, S. Chapman, M. Charlton, S. S. El Nasr, J. Fajans, M. C. Fujiwara, D. R. Gill, J. S. Hangst, W. N. Hardy, R. S. Hayano, M. E. Hayden, A. J. Humphries, R. Hydomako, L. V. Jørgensen, S. J. Kerrigan, L. Kurchaninov, R. Lambo, N. Madsen, P. Nolan, K. Olchanski, A. Olin, A. P. Povilus, P. Pusa, E. Sarid, D. M. Silveira, J. W. Storey, R. I. Thompson, D. P. van der Werf, Y. Yamazaki, and A. Collaboration, "Antiproton, positron, and electron imaging with a microchannel plate/phosphor detector," Rev. Sci. Instrum. **80**, 123701 (2009).
[33]G. Costantini, L. Giorleo, G. Gosta, M. Leali, V. Mascagna, S. Migliorati, M. Prest, F. Ronchetti, L. Solazzi, E. Vallazza, and L. Venturelli, "The upgrade of the asacusa scintillating bar detector for antiproton annihilation measurements," J. Inst. **18**, P04013 (2023).
[34]Y. Nagata, N. Kuroda, C. Sauerzopf, B. Kolbinger, C. Malbrunot, A. Capon, P. Dupre, B. Radics, M. Tajima, C. Kaga, M. Leali, E. Lodi Rizzini, V. Mascagna, O. Massiczek, T. Matsudate, M. Simon, H. Breuker, H. Higaki, Y. Kanai, Y. Matsuda, L. Venturelli, E. Widmann, and Y. Yamazaki, "The development of the antihydrogen beam detector: Toward the three dimensional tracking with a BGO crystal and a hodoscope," JPS Conf. Proc. **18**, 011038 (2017).
[35]S. Maury, W. Oelert, W. Bartmann, P. Belochitskii, H. Breuker, F. Butin, C. Carli, T. Eriksson, S. Pasinelli, and G. Tranquille, "ELENA: The extra low energy anti-proton facility at CERN," Hyperfine Interact. **229**, 105–115 (2014).
[36]C. Amsler, H. Breuker, M. Bumbar, S. Chesnevskaya, G. Costantini, R. Ferragut, M. Giammarchi, A. Gligorova, G. Gosta, H. Higaki, M. Hori, E. Hunter, C. Killian, V. Kraxberger, N. Kuroda, A. Lanz, M. Leali, G. Maero, C. Malbrunot, V. Mascagna, Y. Matsuda, V. Mäckel, S. Migliorati, D. Murtagh, Y. Nagata, A. Nanda, L. Nowak, M. Romé, M. Simon, M. Tajima, V. Toso, S. Ulmer, L. Venturelli, A. Weiser, E. Widmann, and Y. Yamazaki, "Injection and capture of antiprotons in a penning–malmberg trap using a drift tube accelerator and degrader foil," Nucl. Instrum. Methods Phys. Res., Sect. A **1065**, 169529 (2024).
[37]G. B. Andresen, W. Bertsche, P. D. Bowe, C. C. Bray, E. Butler, C. L. Cesar, S. Chapman, M. Charlton, J. Fajans, M. C. Fujiwara, R. Funakoshi, D. R. Gill, J. S. Hangst, W. N. Hardy, R. S. Hayano, M. E. Hayden, R. Hydomako, M. J. Jenkins, L. V. Jørgensen, L. Kurchaninov, R. Lambo, N. Madsen, P. Nolan, K. Olchanski, A. Olin, A. Povilus, P. Pusa, F. Robicheaux, E. Sarid, S. Seif El Nasr, D. M. Silveira, J. W. Storey, R. I. Thompson, D. P. van der Werf, J. S. Wurtele, and Y. Yamazaki, "Compression of antiproton clouds for antihydrogen trapping," Phys. Rev. Lett. **100**, 123701 (2008).
[38]A. Lanz, C. Amsler, H. Breuker, M. Bumbar, S. Chesnevskaya, G. Costantini, R. Ferragut, M. Giammarchi, A. Gligorova, G. Gosta, H. Higaki, C. Killian, V. Kraxberger, N. Kuroda, M. Leali, G. Maero, C. Malbrunot, V. Mascagna, Y. Matsuda, V. Mäckel, S. Migliorati, D. Murtagh, A. Nanda, L. Nowak, F. Parnefjord Gustafsson, S. Rheinfrank, M. Romé, M. Simon, M. Tajima, V. Toso, S. Ulmer, L. Venturelli, A. Weiser, E. Widmann, Y. Yamazaki, and J. Zmeskal, "Upgrade of the positron system of the ASACUSA-Cusp experiment," arXiv:2307.06133 (2023).
[39]E. D. Hunter, M. Bumbar, C. Amsler, M. Bayo, H. Breuker, M. Cerwenka, G. Costantini, R. Ferragut, M. Giammarchi, A. Gligorova, G. Gosta, H. Higaki, C. Killian, V. Kraxberger, N. Kuroda, A. Lanz, M. Leali, G. Maero, C. Malbrunot, V. Mascagna, Y. Matsuda, S. Migliorati, D. J. Murtagh, A. Nanda, L. Nowak, M.

26 October 2026 11:25:02

© Author(s) 2026

Romé, R. Sheldon, M. C. Simon, M. Tajima, V. Toso, S. Ulmer, L. Venturelli, A. Weiser, E. Widmann, and Y. Yamazaki, "Best practices for the manufacture of antimatter atoms," in Proceedings of International Conference on Exotic Atoms and Related Topics and Conference on Low Energy Antiprotons—PoS(EXA-LEAP2024), 2025.
[40]M. Ahmadi, B. Alves, C. Baker, W. Bertsche, A. Capra, C. Carruth, C. Cesar, M. Charlton, S. Cohen, R. Collister, S. Eriksson, A. Evans, N. Evetts, J. Fajans, T. Friesen, M. Fujiwara, D. Gill, J. Hangst, W. Hardy, M. Hayden, C. Isaac, M. Johnson, S. Jones, S. Jonsell, L. Kurchaninov, N. Madsen, M. Mathers, D. Maxwell, J. McKenna, S. Menary, T. Momose, J. Munich, K. Olchanski, A. Olin, P. Pusa, C. O. Rasmussen, F. Robicheaux, R. Sacramento, M. Sameed, E. Sarid, D. Silveira, C. So, G. Stutter, T. Tharp, J. Thompson, R. Thompson, D. van der Werf, J. Wurtele, and A. Collaboration, "Enhanced control and reproducibility of non-neutral plasmas," Phys. Rev. Lett. **120**, 025001 (2018).
[41]G. B. Andresen, M. D. Ashkezari, M. Baquero-Ruiz, W. Bertsche, P. D. Bowe, E. Butler, C. L. Cesar, S. Chapman, M. Charlton, J. Fajans *et al.*, "Evaporative cooling of antiprotons to cryogenic temperatures," Phys. Rev. Lett. **105**, 013003 (2010).
[42]A. A. Kabantsev, C. F. Driscoll, T. J. Hilsabeck, T. M. O'Neil, and J. H. Yu, "Trapped-particle asymmetry modes in single-species plasmas," Phys. Rev. Lett. **87**, 225002 (2001).
[43]D. H. E. Dubin, "Superbanana transport in the collisional heating of a plasma column forced across a squeeze potential," Phys. Plasmas **24**, 112120 (2017).
[44]F. Anderegg, M. Affolter, D. H. E. Dubin, and C. F. Driscoll, "Plasma heating due to cyclic diffusion across a separatrix," Phys. Rev. Lett. **123**, 105002 (2019).
[45]N. Higashi, A. Sanpei, and H. Himura, "The effect of a nested trap on the orbital motion of a pure electron plasma," Phys. Plasmas **32**, 122104 (2025).
[46]S. Jonsell, D. P. v d Werf, M. Charlton, and F. Robicheaux, "Simulation of the formation of antihydrogen in a nested penning trap: Effect of positron density," J. Phys. B **42**, 215002 (2009).
[47]S. Jonsell and M. Charlton, "Formation of antihydrogen beams from positron–antiproton interactions," New J. Phys. **21**, 073020 (2019).
[48]M. E. Glinsky and T. M. O'Neil, "Guiding center atoms: Three-body recombination in a strongly magnetized plasma," Phys. Fluids B **3**, 1279–1293 (1991).
[49]J. R. Danielson, T. R. Weber, and C. M. Surko, "Extraction of small-diameter beams from single-component plasmas," Appl. Phys. Lett. **90**, 081503 (2007).
[50]A. Zhong, J. Fajans, and J. S. Wurtele, "Shot-noise-induced lower temperature limit of the nonneutral plasma parallel temperature diagnostic," EPJ Tech. Instrum. **11**, 6 (2024).
[51]C. F. Driscoll, "Observation of an unstable l=1 diocotron mode on a hollow electron column," Phys. Rev. Lett. **64**, 645–648 (1990).
[52]G. W. Mason and R. L. Spencer, "Simulations of the instability of the m = 1 self-shielding diocotron mode in finite-length non-neutral plasmas," Phys. Plasmas **9**, 3217–3224 (2002).
[53]T. J. Hilsabeck and T. M. O'Neil, "Finite length diocotron modes," Phys. Plasmas **8**, 407–422 (2001).
[54]E. D. Hunter (2025). "Data and analysis for optimizing antihydrogen production in ASACUSA's Cusp trap," Zenodo. https://doi.org/10.5281/zenodo.17434838
[55]R. Akbari, L. de Araujo Azevedo, C. J. Baker, W. Bertsche, N. M. Bhatt, G. Bonomi, A. Capra, I. Carli, C. L. Cesar, M. Charlton, A. Cridland Mathad, A. Del Vincio, D. Duque Quiceno, S. J. Eriksson, A. Evans, J. Ewins, J. Fajans, T. Friesen, M. C. Fujiwara, L. M. Golino, M. B. Gomes Gonçalves, J. S. Hangst, M. E. Hayden, D. Hodgkinson, C. A. Isaac, A. J. U. Jimenez, S. A. Jones, S. Jonsell, N. Madsen, V. R. Marshall, J. T. K. McKenna, T. Momose, J. Nauta, A. N. Oliveira, J. Peszka, A. Powell, C. O. Rasmussen, T. Robertson-Brown, F. Robicheaux, R. L. Sacramento, E. Sarid, J. Schoonwater, D. M. Silveira, J. Singh, G. Smith, C. So, S. Stracka, J. Suh, A. G. Swadling, T. D. Tharp, K. A. Thompson, R. I. Thompson, E. Thorpe-Woods, M. Urioni, D. P. van der Werf, P. Woosaree, and J. S. Wurtele, "Be^+ assisted, simultaneous confinement of more than 15000 antihydrogen atoms," Nat. Commun. **16**, 10106 (2025).
[56]M. Diermaier, C. B. Jepsen, B. Kolbinger, C. Malbrunot, O. Massiczek, C. Sauerzopf, M. C. Simon, J. Zmeskal, and E. Widmann, "In-beam measurement of the hydrogen hyperfine splitting and prospects for antihydrogen spectroscopy," Nat. Commun. **8**, 15749 (2017).
[57]N. Madsen and M. Charlton, "On the formation of antihydrogen beams using travelling optical lattices," New J. Phys. **23**, 073003 (2021).
[58]L. T. Evans, "Phenomenology of creation of antihydrogen and measurement of antihydrogen properties," Ph.D. thesis (University of California, Berkeley, 2016).
[59]J. Fajans, "Non-neutral plasma equilibria, trapping, separatrices, and separatrix crossing in magnetic mirrors," Phys. Plasmas **10**, 1209–1214 (2003).
[60]A. Christensen, "Exploiting electron magnetron motion in a Penning-Malmberg trap to measure patch potentials, misalignment, and magnetic fields," Ph.D. thesis (University of California, Berkeley, 2024).
[61]A. Knights and P. Coleman, "Secondary electron emission from Ag(100) stimulated by positron and electron impact," Appl. Surf. Sci. **85**, 43–48 (1995).
[62]N. Overton and P. G. Coleman, "Measurement of the energy spectrum of secondary electrons ejected from solids by positron impact," Phys. Rev. Lett. **79**, 305–308 (1997).

26 October 2026 11:25:02

© Author(s) 2026